ReS_2 Nanosheets with In Situ Formed Sulfur Vacancies for Efficient and Highly Selective Photocatalytic CO_2 Reduction

Yanzhao Zhang, Dazhi Yao, Bingquan Xia, Haolan Xu, Youhong Tang, Kenneth Davey, Jingrun Ran, and Shi-Zhang Qiao**

Artificial photosynthesis can provide valuable fuels and positively impact greenhouse effects, via transforming carbon dioxide (CO_2) and water (H_2O) into hydrocarbons using semiconductor-based photocatalysts. However, the inefficient charge-carrier dissociation and transportation as well as the lack of surface active sites are two major drawbacks to boosting their activity and selectivity in photocatalytic CO_2 reduction. Recently, ReS_2 has received tremendous attention in the photocatalysis area due to its intriguing physicochemical properties. Nevertheless, the application of ReS_2 in photocatalytic CO_2 reduction is scarcely covered. Herein, a heterojunction formed between ReS_2 nanosheets and CdS nanoparticles is reported, achieving an apparently raised CO production of 7.1 μmol g^{-1} and high selectivity of 93.4%. The as-prepared ReS_2/CdS heterojunction exhibits strengthened visible-light absorption, high-efficiency electron–hole pair separation/transfer, and increased adsorption/activation/reduction of CO_2 on in situ created sulfur vacancies of ReS_2, thus all favoring CO_2 photoreduction. These are corroborated by advanced characterization techniques, e.g., synchrotron-based X-ray absorption near-edge structure, and density functional theory–based computations. The findings will be of broad interest in practical design and fabrication of surface active sites and semiconductor heterojunctions for applications in catalysis, electronics, and optoelectronics.

1. Introduction

CO_2 emission leads to severe global greenhouse effect. Therefore, various strategies have been developed to relieve this process, including CO_2 fixation and cyclic utilization.[1–4] Meanwhile, the application of clean and renewable energy to fix CO_2 can not only promote the carbon cycle but also relieve the global energy crisis. Semiconductor-based photocatalytic carbon dioxide (CO_2) conversion represents a carbon-neutral and sustainable strategy to generate fuels and chemicals using renewable and clean solar energy.[1–5] This process is fundamentally impacted by three steps: 1) light absorption to excite semiconductor-based photocatalysts, 2) photogenerated electron–hole pair separation and transfer efficiency, and 3) redox reactions on the surface of the photocatalyst.[6,7] To improve photocatalytic CO_2 reduction, researchers have generally focused on approaches including introducing defects in the crystal lattice,[8–13] loading metal cocatalysts,[14,15] exposing highly active facets,[16,17] and fabricating heterojunctions.[7,18] Among these, forming heterojunctions in composites is deemed as an effective strategy due to efficient suppression of charge carrier recombination and highly promoted migration efficiency.[19,20] Some cocatalysts broaden the light absorption spectrum to utilize long-wavelength light.[21,22] However, CO_2 molecules are highly thermodynamically stable with a bond energy of 750 kJ mol^{-1} for C—O.[6] This implies that the dissociation of CO_2 requires high energy via conventional methods.[6] The activation of CO_2 molecules on the surface of photocatalysts relies on various active sites, e.g., functional groups, frustrated Lewis pairs, single atoms and vacancies. These possess an affinity for CO_2 and water (H_2O) adsorption and activation. These are however rare on the perfect surfaces

---

Y. Zhang, D. Yao, B. Xia, Dr. K. Davey, Dr. J. Ran, Prof. S.-Z. Qiao
School of Chemical Engineering and Advanced Materials
The University of Adelaide
Adelaide, SA 5005, Australia
E-mail: jingrun.ran@adelaide.edu.au; s.qiao@adelaide.edu.au

The ORCID identification number(s) for the author(s) of this article can be found under https://doi.org/10.1002/smsc.202000052.

DOI: 10.1002/smsc.202000052

Prof. H. Xu
Future Industries Institute
University of South Australia
Adelaide, SA 5095, Australia

Prof. Y. Tang
Center for Nanoscale Science and Technology
School of Computer Science
Engineering, and Mathematics
Flinders University
Adelaide, SA 5042, Australia

of photocatalysts. The deliberate creation of active sites on the surfaces of photocatalysts is therefore a major research approach to practically realize effective photocatalysis.[6]

Transition metal dichalcogenides (TMDs) have received significant attention in catalysis, rechargeable batteries, and sensing devices.[23–28] For example, Zhou et al. reported that FeS ultrathin nanosheets on a carbon fiber cloth achieved highly efficient hydrogen evolution due to the phase transition triggered by illumination at room temperature.[29] Similarly, Fu et al. prepared $MoReS_3$ with a layered structure, a new type of TMDs, and it showed excellent hydrogen evolution in electrocatalysis.[30] As a new type of TMDs, ReS_2 has been studied in photocatalytic hydrogen evolution (PHE), both experimentally and theoretically.[31–38] Zhang et al.[34] reported that ReS_2 exhibited significant performance in PHE, a two-electron catalytic reaction. This is because free electrons are captured by tightly bound excitons to form trions that constrain recombination and thereby promote performance. The corresponding computation indicates that the adsorption energy of the H atoms exhibits a small absolute value (-0.5 eV), revealing the highly efficient PHE performance. With a narrow bandgap of 1.7 eV, ReS_2 possesses strong absorption in the visible-light range, thus benefiting photocatalytic activity. In addition, ReS_2 exhibits an automatic transition of hydrophobicity–hydrophilicity before and following visible-light illumination.[35] This is because defects on its surface change the adsorption configuration of H_2O and oxygen (O_2) to form hydroxyl groups leading to the transmission of hydrophilicity.[35] This adsorption configuration impacts adsorption of CO_2 and H_2O in CO_2 photoreduction. Zhou et al.[36] reported that Re sites can absorb hydrogen as the intermediate for CO_2 hydrogenation. Findings suggest ReS_2 nanosheets (NSs) are a potential photocatalyst for CO_2 reduction. A drawback however with most TMDs is that the reactive sites are located at the edge of the NSs, because of the hanging bond created by breakage of the bond between the transmitting metal and sulfur. These limited active sites on the edge and inert surface elsewhere are a significant impediment to applying TMDs as photocatalysts. Therefore, the activation of the inert surface through the introduction of defects on ReS_2 NSs is regarded as an effective strategy to boost their photocatalytic performance.

Herein, we report a simple self-assembly approach to synthesize a heterojunction composed of ReS_2 NSs and CdS nanoparticles (NPs) for photocatalytic CO_2 reduction. The optimized ReS_2/CdS heterostructure exhibits a boosted photocatalytic CO_2-to-CO conversion activity of 7.1 μmol g^{-1} accompanied by a high selectivity of 93.4%. The enhanced performance is aroused by high-efficiency interfacial charge transfer between ReS_2 and CdS as well as in situ formed sulfur vacancies on the ReS_2 surface. Results from advanced characterizations, e.g., synchrotron-based X-ray absorption near-edge structure (XANES), together with X-ray photoelectron spectroscopy (XPS), confirm the strong electronic coupling between ReS_2 and CdS. Density functional theory (DFT)-based computations highlight the adsorption and activation of CO_2 on the ReS_2 surface with in situ formed sulfur vacancies based on electron transfer and change in C—O bond length and angle. Our work will be of immediate practical interest to a wide range of researchers for the design and synthesis of nanostructured materials in the field of energy conversion and storage.

2. Results and Discussion

ReS_2 NSs were prepared by exfoliating commercial bulk ReS_2 under ultrasonication in deionized water, and CdS NPs were fabricated by a hydrothermal method. Then, the heterojunctions of ReS_2 and CdS were synthesized by physical mixing. The as-prepared samples were denoted as CdS, CR4, CR8 and CR12, respectively, according to the added volumes of ReS_2 NSs suspension (0, 4, 8 and 12 mL, respectively). The X-ray diffraction (XRD) patterns of all the as-prepared samples are shown in Figure S1, Supporting Information. The pattern displayed is ascribed to cubic-phase CdS (PDF #10-0454). A weak peak at 14.6° is attributed to the presence of ReS_2 NSs. The intensity of this peak is enhanced with increasing content of ReS_2 in the heterojunction. No apparent alteration of peak positions and intensities is observed for cubic-phase CdS after its combination with ReS_2, suggesting the weak interaction formed via physical mixing at room temperature does not change the crystal structure.

Furthermore, the morphologies and microstructures of CdS NPs, ReS_2 NSs, and CR12 are characterized by aberration-corrected high-angle annular dark field scanning transmission electron microscopy (HAADF-STEM), transmission electron microscopy (TEM), and HAADF-STEM elemental mapping. The HAADF-STEM image of CdS NPs (**Figure 1**a) exhibits a lattice spacing value of 0.33 nm, ascribed to the (111) facet of cubic-phase CdS. In addition, the HAADF-STEM image of a ReS_2 NSs (Figure 1b) shows the typical Re_4 diamond chain (DC) structure (yellow dot line square). The spacing values between the Re_4 diamond in the *a* [100] and *b* [010] directions are 0.35 and 0.31 nm, respectively (Figure 1b). This is also displayed in the simulated atomic structure of the ReS_2 monolayer (Figure 1c). It is reported that Re_4 DCs can act as reactive sites for water splitting. This is because these favor water adsorption and activation, and possibly assist proton transfer to participate in CO_2 photoreduction.[33,34] The thickness of the ReS_2 NSs was further confirmed to be $\approx$6.5 nm using atomic force microscopy (AFM; Figure 1d). The ultrathin thickness of the ReS_2 NSs not only endows them with a large surface area to form strong electronic coupling with other materials, but also increases the number of exposed active sites toward catalytic reactions. The combination of a ReS_2 NSs and CdS NPs in CR12 is shown in Figure 1e. Moreover, the HAADF-STEM image and the corresponding energy dispersive X-ray (EDX) elemental mapping images further corroborate the hybridization of the ReS_2 NSs and CdS NPs (Figure 1f) in CR12. The colors red, yellow, and green in Figure 1f represent, respectively, the distribution of Cd, S, and Re elements, in agreement with the HAADF-STEM image.

Moreover, both surface-sensitive XPS and synchrotron-based XANES were conducted to disclose the interactions between CdS and ReS_2 in CR12. The high-resolution Re 4*f* XPS spectrum for CR12 (**Figure 2**a) showed a shift of $\approx$0.5 eV toward the direction of lower binding energy compared with that for pure ReS_2 (Figure 2b), suggesting electron transfer from CdS to ReS_2 in CR12. In addition, the high-resolution XPS spectrum of Cd 3*d* for CR12 shifts to the direction of higher binding energy (Figure 2c), also indicating the electron migration from CdS to ReS_2 in CR12. Furthermore, synchrotron-based XANES was performed (Figure 2d). The S K-edge XANES of CR12 indicates

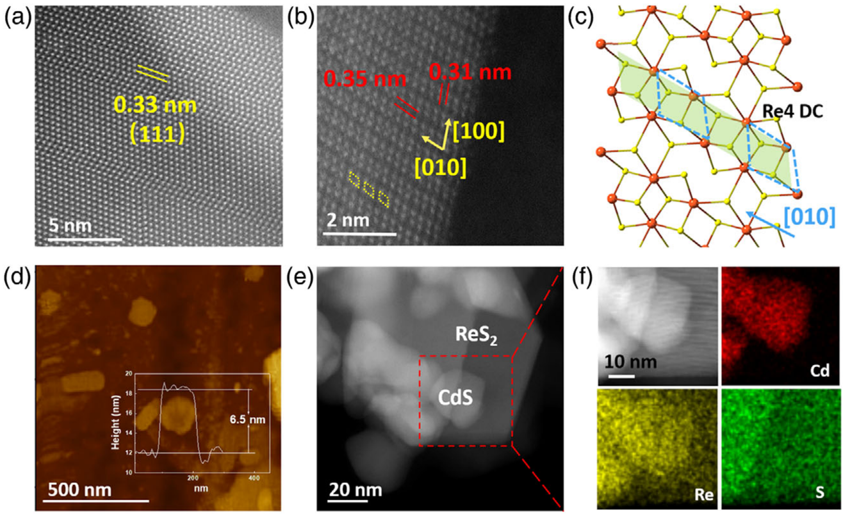

Figure 1. Aberration-corrected HAADF-STEM images of a) CdS NPs and b) ReS_2 NSs. c) Simulated model for ReS_2. The red and yellow colored spheres denote Re and S, respectively, and the blue-dotted line denotes the Re_4 diamond chain. d) AFM image of ReS_2 NSs and measured thickness of ReS_2. e) TEM of ReS_2 NSs and CdS NPs. f) EDX mapping of CR12 from red-dotted rectangle of (e).

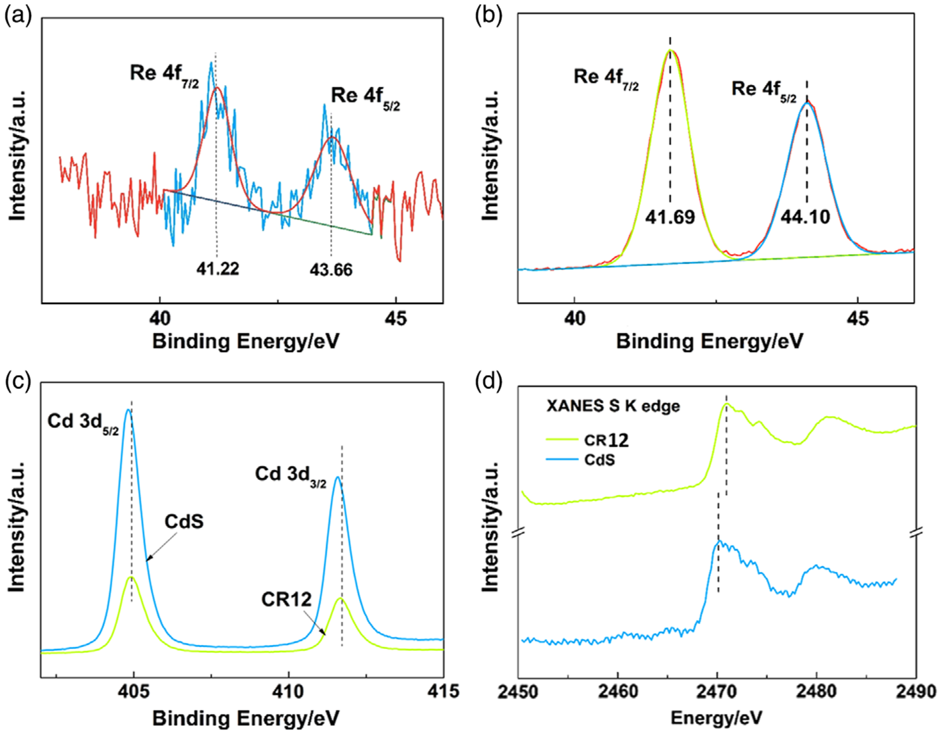

Figure 2. a) High-resolution XPS spectrum of Re 4*f* for CR12. b) High-resolution XPS spectrum of Re 4*f* for ReS_2. c) High-resolution XPS spectrum of Cd 3*d* for CdS and CR12. d) XANES S K edge of CdS and CR12.

a shift toward high photon energy direction, in comparison to that for CdS. This also supports the electron transfer from CdS to ReS_2 in CR12.

Solid–gas phase photocatalytic CO_2 reduction activities of the as-prepared samples were examined under visible-light irradiation ($\lambda \geq 420$ nm). As shown in **Figure 3**a, CdS shows a limited photocatalytic CO_2 reduction activity with CO and CH_4 production of 2.3 and 1.1 μmol g^{-1} over 7 h (Figure S2, supporting information). The coupling of ReS_2 and CdS (CR4, CR8, and CR12) leads to apparent enhancement of both activity and selectivity in visible-light-driven CO_2-to-CO conversion (Figure 3a). In particular, CR12 shows the highest photocatalytic CO_2-to-CO conversion activity of 7.1 μmol g^{-1} and selectivity 93.4%, ≈309%, and 138% times higher than those of CdS alone.

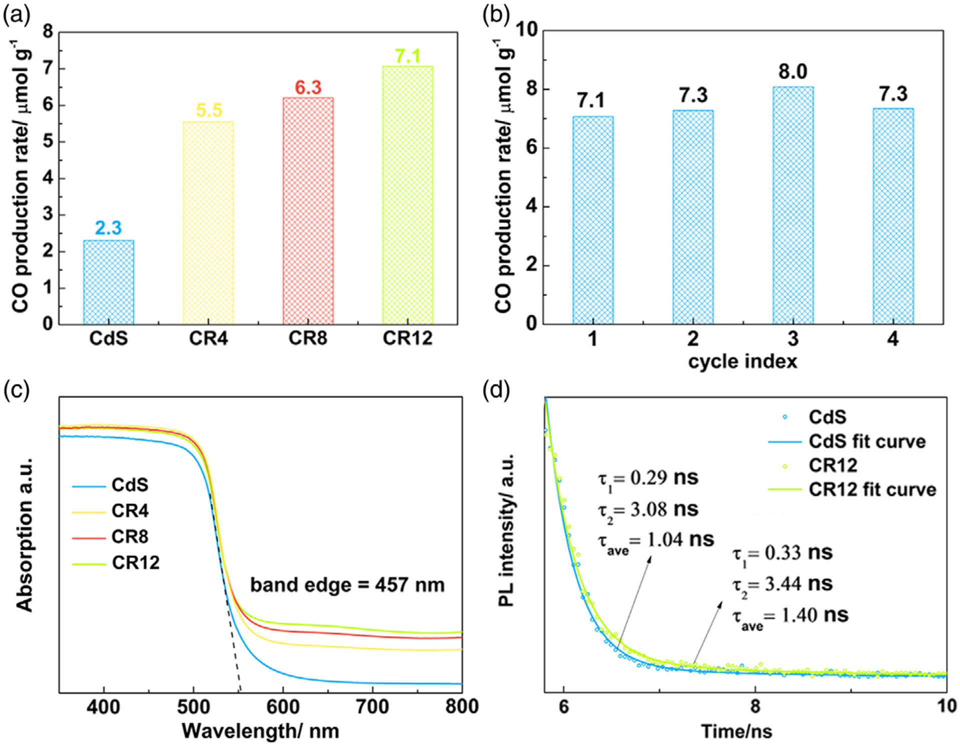

Figure 3. a) Photocatalytic CO_2 reduction activities of CdS, CR4, CR8, and CR12 under visible-light illumination ($\lambda \geq 420$ nm). b) Photocatalytic CO_2 reduction activity of CR12 recycle test with 7 h per cycle test. c) UV–vis diffuse reflectance spectroscopy and band edge for CdS, CR4, CR8, and CR12. d) TSPL spectra for CdS and CR12.

This result for the first time demonstrates that coupling with a ReS_2 NS could significantly boost both activity and selectivity in photocatalytic CO_2-to-CO conversion. In addition, we conducted three blank experiments under the same conditions but purged with ultra-high-purity argon gas instead of CO_2, without visible-light illumination and without a photocatalyst, respectively. These contrast experiments show no photocatalytic CO_2 conversion performance, suggesting that the products (CO and CH_4) are generated from photoinduced CO_2 conversion. Furthermore, the stability of CR12 was studied via four-cycle testing with 7 h per cycle (Figure 3b). No apparent deterioration in photocatalytic CO_2 reduction performance of CR12 was found over a 28 h test. The TEM image and EDX spectrum (Figure S3, Supporting Information) of CR12 after photocatalytic CO_2 reduction exhibited no obvious difference from those before reaction. This finding suggests that no apparent change in morphology and chemical composition of CR12 occurs after the 28 h photocatalytic reaction.

To further investigate the origin of the enhanced activity and selectivity, as well as the reaction mechanism in CR12 for photocatalytic CO_2 reduction, both experimental characterizations and DFT-based theoretical calculations were conducted. The light absorption capacity was studied by UV–vis diffuse reflectance spectroscopy. As shown in Figure 3c, increased absorption in the range of 460–800 nm is attributed to the presence of ReS_2 NSs. However, the adsorption edge of CR12 (457 nm) does not display any shift. This finding suggests that the bandgap (2.24 eV) is not changed following combination with the ReS_2 NSs. The bandgap of ReS_2 NSs is 1.7 eV (Figure S4, Supporting Information). This induces the "bulge" at ≈600–800 nm in the UV–vis spectrum of CR12. Such an improved visible-light absorption probably contributes to the raised activity in photocatalytic CO_2 reduction.

A range of characterization methods, e.g., steady-state photoluminescence (PL) spectroscopy, transient-state photoluminescence (TSPL) spectroscopy, electrochemical impedance spectroscopy (EIS), and transient photocurrent (TPC) density measurement, were executed to probe the efficiency of charge-carrier separation and transportation. The steady-state PL (Figure S5, Supporting Information) intensity of CR12 is significantly lower than that of CdS. This finding is attributed to the oppressed charge-carrier recombination after coupling with the ReS_2 NSs in CR12. After fitting of the TSPL curves in Figure 3 d, elongated lifetimes of charge carriers ($\tau_1 = 0.33$ ns; $\tau_2 = 3.44$ ns; $\tau_{ave} = 1.40$ ns) for CR12 were observed, in comparison to those for CdS ($\tau_1 = 0.29$ ns; $\tau_2 = 3.08$ ns; $\tau_{ave} = 1.04$ ns). This also supports the more effective dissociation and migration of photogenerated electrons and holes in CR12. Furthermore, the EIS spectra (Figure S6a, Supporting Information) exhibit a smaller semicircle radius for the Nyquist plot together with a decreased charge-transfer resistance ($R_t = 4672\ \Omega$) for CR12 in contrast with that of CdS ($R_t = 4830\ \Omega$). This finding suggests a faster charge-carrier migration rate in CR12. In addition, CR12 exhibits a greater TPC density than CdS (Figure S6b, Supporting Information). This also confirms the more efficient dissociation of light-induced excitons, in agreement with the earlier PL and EIS spectra results.

To investigate the CO_2 adsorption, activation, and reduction process, XPS and Raman characterizations were conducted for pristine ReS_2, RS1, RS2, and RS3 (see details in Section 1.5, Supporting Information). The C 1*s* peaks in **Figure 4**a–c mainly consist of a peak located at 284.6 eV, ascribed to the contaminated carbon. All other peaks were calibrated using this peak. After deconvolution of the C 1*s* peaks in Figure 4a–c, four satellite peaks can be obtained and attributed to C—OH, *COOH, b-CO_2 (chemisorbed and bent CO_2), and l-CO_2 (physisorbed and linear CO_2), respectively.[39] Among these adsorption configurations, *COOH is deemed as the precursor for CO, consistent with the major product (CO) of this work.[40,41] The contents (mol%) acquired based on the areas of four satellite C 1*s* peaks are provided in Table S1, Supporting Information). RS1 shows the highest contents of C 1*s* peaks associated with *COOH and b-CO_2, in comparison to RS2 and RS3. This is because the water vapor can facilitate the adsorption of CO_2.[42–44] The aforementioned results indicate that the adsorption of CO_2 on the surface of the ReS_2 NSs is obviously enhanced by visible-light illumination. To further study the key role of illumination on CO_2 adsorption, the high-resolution XPS spectra of S 2*p* for pristine ReS_2 NSs, RS1, RS2, and RS3 were collected. The ReS_2 NSs exhibits two peaks located at 162.05 and 163.18 eV, ascribed to the S $2p_{3/2}$ and S $2p_{1/2}$ (Figure S7, Supporting Information). In comparison, after light illumination, satellite peaks located at 162.7 and 163.85 eV appear (Figure 4d–f), attributed to the presence of sulfur vacancy induced by visible-light illumination. Moreover, the high-resolution Re 4*f* XPS spectrum (Figure S7, Supporting Information) of the pristine ReS_2 NSs only exhibits two peaks at 41.65 and 44.06 eV, attributed to the Re $4f_{7/2}$ and Re $4f_{5/2}$ peaks, respectively. In comparison, Re 4*f* satellite peaks located at lower binding energy positions are observed in the high-resolution Re 4*f* XPS spectra of RS1, RS2, and RS3 (Figure S8a–c, Supporting Information), also implying the presence of sulfur vacancies in ReS_2 after light illumination. Furthermore, the aberration-corrected HAADF-STEM images of RS1 and pristine ReS_2 are displayed in Figure S9a,b,

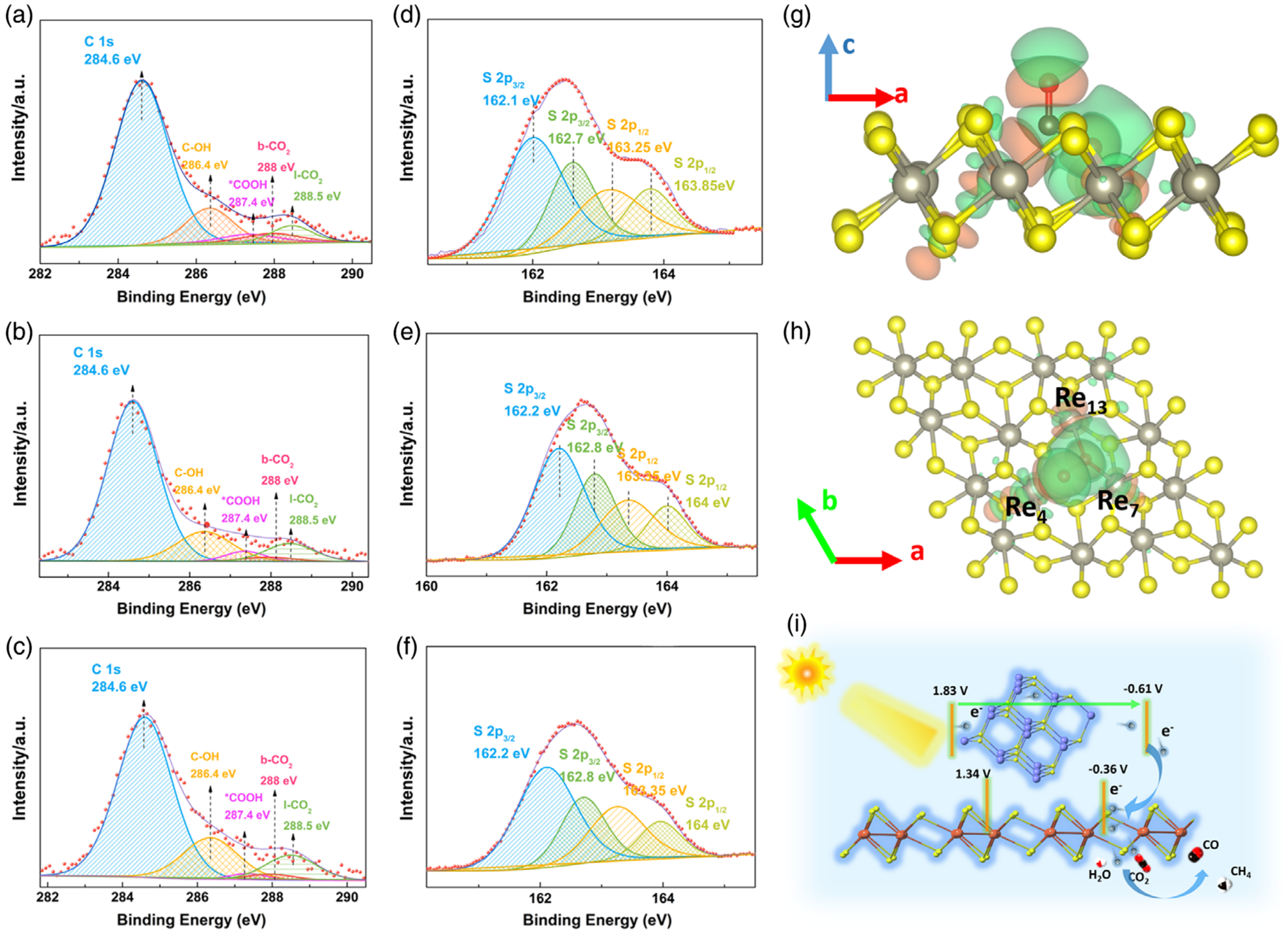

Figure 4. a,d) High-resolution XPS spectrum for C 1s and S 2*p* for RS1. b,e) High-resolution XPS spectrum for C 1s and S 2*p* for RS2. c,f) High-resolution XPS spectrum for C 1s and S 2*p* for RS3. g) Side-view (elevation) and h) top-view (plan) of the electron density distribution of absorbed CO_2 on V_s-ReS_2. The red, yellow, gray, and brown colored spheres denote O, S, Re, and C atoms, respectively. The isosurface value is set to 0.002e $Å^{-3}$. i) Schematic of photocatalytic CO_2 reduction in CR12 system under visible-light illumination ($\lambda \geq 420$ nm). The purple, red, yellow, orange, white, and black colored spheres denote Cd, O, S, Re, H, and C atoms, respectively.

respectively. In contrast to pristine ReS_2, RS1 exhibits more defects, e.g., vacancies and pores, on its surface after the light illumination. This finding is in agreement with the aforementioned XPS results.

These findings are further corroborated by the Raman spectroscopy characterization. Pristine ReS_2 displays a typical E_g-like peak at $\approx 305\,cm^{-1}$ (Figure S10, Supporting Information). In contrast, RS1, RS2, and RS3 all exhibit a blueshift of the E_g-like peak. This might be caused by the presence of a sulfur vacancy leading to the mass fluctuation at the S position. In addition, RS1, RS2, and RS3 all exhibit peaks at $\approx 1271\,cm^{-1}$, ascribed to *COOH (Figure S11, Supporting Information).[40,41] In particular, the highest *COOH peak intensity is observed for RS1, compared to those of RS2 and RS3, in coincidence with the aforementioned XPS results (Table S1, Supporting Information). These findings were reinforced in the Fourier transform infrared spectroscopy (FTIR) spectra (Figure S12, Supporting Information). The bands at $1620\,cm^{-1}$ are attributed to *COOH and the bands at $1404\,cm^{-1}$ to the symmetric (O—C—O) vibration, indicating the presence of adsorbed CO_2 molecules on the surface of the photocatalyst. These findings are consistent with those from the XPS results.

To verify the possible CO_2 activation on the ReS_2 with the sulfur vacancy (V_s-ReS_2), DFT-based theoretical computation was conducted to determine the adsorption of CO_2 and the local electronic structure. As shown in Figure S13, Supporting Information, the atomic structures for V_s-ReS_2 were constructed and optimized. The adsorption behavior of CO_2 on the surface of V_s-ReS_2 was studied (Figure 4g,h). The adsorption energy (E_{ad}) of CO_2 on V_s-ReS_2 was found to be -0.82 eV. This value demonstrates that the chemisorption of CO_2 on V_s-ReS_2 is favorable.[45,46] The CO_2 molecule loses linearity to change α(OCO) to 117.9°, and the two C—O_1 and C—O_2 bonds are lengthened to 1.209 and 1.398 Å, respectively, thereby denoting activation of the C═O bond on V_s-ReS_2.[46,47]

Bader charge analysis (Figure S14, Supporting Information) was conducted to study the charge distribution on the CO_2-adsorbed V_s-ReS_2 and to investigate the electronic impact. It was found that Re atoms and C atoms are electron deficient, whereas S atoms and O atoms are negatively charged (Figure S14a, Supporting Information). In particular, Re near a sulfur vacancy (Re_4, Re_7, and Re_{13}) changed more positively when CO_2 was absorbed onto V_s-ReS_2 (Figure S14b, Supporting Information).[38,46,47] Charge density difference was used to visualize the electron transfer behavior. The findings showed that Re and carbon atoms donate charges to oxygen and that they are positively charged.[37,46,47] These findings confirm that V_s-ReS_2 favorably impacts chemisorption and activation of CO_2 and electron transfer between CO_2 and V_s-ReS_2.

Based on the findings from both the experimental studies and theoretical computations, a possible photocatalytic CO_2 reduction mechanism is proposed. The conduction band (CB) and valence band (VB) edge positions of CdS and ReS_2 are estimated via combining their Mott–Schottky plots (Figure S15, Supporting Information) and UV–vis diffuse reflectance spectrum (Figure S5, Supporting Information). As shown in Figure 4i, CdS and ReS_2 form a type I (straddling-type) heterojunction. Under visible-light illumination ($\lambda \geq 420$ nm), the CdS NPs are photoexcited and the electrons transfer from the VB to the CB, whereas the photogenerated holes in the VB of CdS will migrate to the VB of ReS_2, where H_2O molecules are oxidized. Then, photogenerated electrons in the CB of CdS transfer to the CB of ReS_2. The ReS_2 NSs accommodates abundant active sites for the adsorption, activation, and reduction of CO_2 and H_2O to evolve CO and CH_4 (Equation (1)–(3)). The most likely pathways for the CO_2 photoreduction on the CdS/ReS_2 heterojunction are proposed as

$$* + CO_2 + e^- + H^+ \rightarrow COOH^* \tag{1}$$

$$COOH^* + e^- + H^+ \rightarrow CO^* + H_2O \tag{2}$$

$$CO^* \rightarrow * + CO \uparrow \tag{3}$$

The asterisks and vertical arrows, respectively, denote reactive sites and the release of gas.

The presence of ReS_2 NSs in CR12 leads to the apparent enhancement in the selectivity of photocatalytic CO_2-to-CO conversion. This is probably because the electrons in ReS_2 can be captured by tightly bound excitons to form trions consisting of two electrons and one hole,[34] which facilitates the two-electron reduction reaction of CO_2-to-CO conversion rather than the eight-electron reduction reaction of CH_4 production.

3. Conclusions

In summary, we have successfully prepared a heterojunction of ReS_2 NSs and CdS NPs using a facile self-assembly method via physical mixing at room temperature. This nanocomposite exhibits a significantly boosted visible-light photocatalytic CO production of 7.1 μmol g^{-1} together with an increased CO_2-to-CO conversion selectivity of 93.4%. Such an improved photocatalytic performance originates from two factors: 1) intimate electronic interaction advancing efficient photogenerated electron–hole separation and migration and 2) in situ generated sulfur vacancies serving as active sites for CO_2 adsorption, activation, and reduction to CO. These are verified by both state-of-the-art characterizations, e.g., synchrotron-based XANES, and theoretical calculations. Our work demonstrates the promising potency of ReS_2 in light-driven CO_2 reduction and the intriguing opportunities of applying in situ generated anion vacancies of transitional metal dichalcogenides in catalysis, electronics, and optoelectronics.

Supporting Information

Supporting Information is available from the Wiley Online Library or from the author.

Acknowledgements

This work was supported financially by the Australian Research Council (ARC) through the Discovery Project Program (DP160104866, FL170100154, and DE200100629). The authors thank Dr. Ting Gao, University of South Australia, for the XPS testing and Dr. Ashley Slattery, Adelaide Microscopy, The University of Adelaide, for technical assistance. DFT computations within this research were undertaken with the support of supercomputing resources provided by the Phoenix HPC service at the University of Adelaide. Y.Z. acknowledges financial support from the Australian Government Research Training Program Scholarship

(RTP). This research was undertaken on the X-ray absorption spectroscopy beamline at the Australian Synchrotron, part of ANSTO.

Conflict of Interest

The authors declare no conflict of interest.

Keywords

CO_2 photoreduction, heterojunctions, ReS_2, sulfur vacancies, transition metal dichalcogenides

Received: November 15, 2020
Revised: November 30, 2020
Published online: January 15, 2021

[1] S. Solomon, G. K. Plattner, R. Knutti, P. Friedlingstein, *Proc. Natl. Acad. Sci. USA* **2009**, *106*, 1704.
[2] N. S. Lewis, D. G. Nocera, *Proc. Natl. Acad. Sci. USA* **2006**, *103*, 15729.
[3] M. Vermeer, S. Rahmstorf, *Proc. Natl. Acad. Sci. USA* **2009**, *106*, 21527.
[4] P. N. Pearson, M. R. Palmer, *Nature* **2000**, *406*, 695.
[5] M. Meinshausen, N. Meinshausen, W. Hare, S. C. Raper, K. Frieler, R. Knutti, D. J. Frame, M. R. Allen, *Nature* **2009**, *458*, 1158.
[6] Y. Zhang, B. Xia, J. Ran, K. Davey, S. Z. Qiao, *Adv. Energy Mater.* **2020**, *10*, 1903879.
[7] J. Ran, M. Jaroniec, S. Z. Qiao, *Adv. Mater.* **2018**, *30*, 1704649.
[8] Z. Jiang, W. Sun, W. Miao, Z. Yuan, G. Yang, F. Kong, T. Yan, J. Chen, B. Huang, C. An, *Adv. Sci.* **2019**, *6*, 1900289.
[9] S. Sato, T. Morikawa, S. Saeki, T. Kajino, T. Motohiro, *Angew. Chem., Int. Ed.* **2010**, *49*, 5101.
[10] Q. Zhang, T. Gao, J. M. Andino, Y. Li, *Appl. Catal., B* **2012**, *123*, 257.
[11] X. Li, Y. Sun, J. Xu, Y. Shao, J. Wu, X. Xu, Y. Pan, H. Ju, J. Zhu, Y. Xie, *Nat. Energy* **2019**, *4*, 690.
[12] M. Shen, L. Zhang, M. Wang, J. Tian, X. Jin, L. Guo, L. Wang, J. Shi, *J. Mater. Chem. A* **2019**, *7*, 1556.
[13] S. Gao, B. Gu, X. Jiao, Y. Sun, X. Zu, F. Yang, W. Zhu, C. Wang, Z. Feng, B. Ye, *J. Am. Chem. Soc.* **2017**, *139*, 3438.
[14] R. Long, Y. Li, Y. Liu, S. Chen, X. Zheng, C. Gao, C. He, N. Chen, Z. Qi, L. Song, *J. Am. Chem. Soc.* **2017**, *139*, 4486.
[15] X. Cheng, P. Dong, Z. Huang, Y. Zhang, Y. Chen, X. Nie, X. Zhang, *J. CO2 Util.* **2017**, *20*, 200.
[16] Y. Zhang, X. Wang, P. Dong, Z. Huang, X. Nie, X. Zhang, *Green Chem.* **2018**, *20*, 2084.
[17] H. Xu, S. Ouyang, P. Li, T. Kako, J. Ye, *ACS Appl. Mater. Interfaces* **2013**, *5*, 1348.
[18] H. Shi, G. Chen, C. Zhang, Z. Zou, *ACS Catal.* **2014**, *4*, 3637.
[19] S. W. Cao, X. F. Liu, Y. P. Yuan, Z. Y. Zhang, Y. S. Liao, J. Fang, S. C. J. Loo, T. C. Sum, C. Xue, *Appl. Catal. B* **2014**, *147*, 940.
[20] J. Ran, W. Guo, H. Wang, B. Zhu, J. Yu, S. Z. Qiao, *Adv. Mater.* **2018**, *30*, 1800128.
[21] C. Zhao, A. Krall, H. Zhao, Q. Zhang, Y. Li, *Int. J. Hydrogen Energy* **2012**, *37*, 9967.
[22] T. Yui, A. Kan, C. Saitoh, K. Koike, T. Ibusuki, O. Ishitani, *ACS Appl. Mater. Interfaces* **2011**, *3*, 2594.
[23] Y. C. Lin, H. P. Komsa, C. H. Yeh, T. Bjorkman, Z. Y. Liang, C. H. Ho, Y. S. Huang, P. W. Chiu, A. V. Krasheninnikov, K. Suenaga, *ACS Nano* **2015**, *9*, 11249.
[24] Y. Yu, G. H. Nam, Q. He, X. J. Wu, K. Zhang, Z. Yang, J. Chen, Q. Ma, M. Zhao, Z. Liu, F. R. Ran, X. Wang, H. Li, X. Huang, B. Li, Q. Xiong, Q. Zhang, Z. Liu, L. Gu, Y. Du, W. Huang, H. Zhang, *Nat. Chem.* **2018**, *6*, 638.
[25] M. Samadi, N. Sarikhani, M. Zirak, H. Zhang, H. L. Zhang, A. Z. Moshfegh, *Nanoscale Horiz.* **2018**, *3*, 90.
[26] C. Martella, C. Mennucci, A. Lamperti, E. Cappelluti, F. B. de Mongeot, A. Molle, *Adv. Mater.* **2018**, *30*, 1705615.
[27] Q. Yun, Q. Lu, X. Zhang, C. Tan, H. Zhang, *Angew. Chem., Int. Ed.* **2018**, *57*, 626.
[28] X. Wang, G. Li, M. H. Seo, F. M. Hassan, M. A. Hoque, Z. Chen, *Adv. Energy Mater.* **2015**, *5*, 1501106.
[29] G. Zhou, Y. Shan, L. Wang, Y. Hu, J. Guo, F. Hu, J. Shen, Y. Gu, J. Cui, L. Liu, X. Wu, *Nat. Commun.* **2019**, *10*, 399.
[30] Y. Fu, Y. Shan, G. Zhou, L. Long, L. Wang, K. Yin, J. Guo, J. Shen, L. Liu, X. Wu, *Joule* **2019**, *3*, 2955.
[31] K. Keyshar, Y. Gong, G. Ye, G. Brunetto, W. Zhou, D. P. Cole, K. Hackenberg, Y. He, L. Machado, M. Kabbani, A. H. C. Hart, B. Li, D. S. Galvao, A. George, R. Vajtai, C. S. Tiwary, P. M. Ajayan, *Adv. Mater.* **2015**, *27*, 4640.
[32] S. Tongay, H. Sahin, C. Ko, A. Luce, W. Fan, K. Liu, J. Zhou, Y. S. Huang, C. H. Ho, J. Yan, D. Ogletree, S. Aloni, J. Ji, S. Li, J. Li, F. M. Peeters, J. Wu, *Nat. Commun.* **2014**, *5*, 3252.
[33] Q. Zhang, W. Wang, J. Zhang, X. Zhu, L. Fu, *Adv. Mater.* **2018**, *30*, 1704585.
[34] Q. Zhang, W. Wang, J. Zhang, X. Zhu, Q. Zhang, Y. Zhang, Z. Ren, S. Song, J. Wang, Z. Ying, R. Wang, X. Qiu, T. Peng, L. Fu, *Adv. Mater.* **2018**, *30*, 1707123.
[35] W. Wang, J. Zhang, Q. Zhang, S. Wan, X. Zhu, Q. Zhang, W. Wang, Y. Zhang, Y. Liu, L. Fu, *Adv. Mater.* **2018**, *30*, 1804559.
[36] Y. Zhou, E. Song, J. Zhou, J. Lin, R. Ma, Y. Wang, W. Qiu, R. Shen, K. Suenaga, Q. Liu, J. Wang, Z. Liu, J. Liu, *ACS Nano* **2018**, *12*, 4486.
[37] B. Chen, H. Li, H. Liu, X. Wang, F. Xie, Y. Deng, W. Hu, K. Davey, N. Zhao, S. Z. Qiao, *Adv. Energy Mater.* **2019**, *30*, 1970117.
[38] J. Pan, X. Zhou, J. Zhong, J. Hu, *Phys. Lett. A*, **2019**, *31*, 125883.
[39] M. Favaro, H. Xiao, T. Cheng, W. A. Goddard, J. Yano, E. J. Crumlin, *Proc. Natl. Acad. Sci. USA* **2017**, *114*, 6706.
[40] A. Vasileff, X. Zhi, C. Xu, L. Ge, Y. Jiao, Y. Zheng, S. Z. Qiao, *ACS Catal.* **2019**, *9*, 9411.
[41] N. J. Firet, W. A. Smith, *ACS Catal.* **2017**, *7*, 606.
[42] A. O. Yazaydin, A. I. Benin, S. A. Faheem, P. Jakubczak, J. J. Low, R. R. Willis, R. Q. Snurr, *Chem. Mater.* **2009**, *21*, 1425.
[43] M. B. Yue, L. B. Sun, Y. Cao, Z. J. Wang, Y. Wang, Q. Yu, J. H. Zhu, *Microporous Mesoporous Mater.* **2008**, *114*, 74.
[44] B. Zhao, Y. X. Pan, C. J. Liu, *Catal. Today* **2012**, *194*, 60.
[45] X. Zhi, Y. Jiao, Y. Zheng, S. Qiao, *Small* **2019**, *15*, 1804224.
[46] R. Khaledialidusti, A. K. Mishra, A. Barnoush, *ACS Omega* **2019**, *4*, 15935.
[47] H. Li, J. Shang, Z. Ai, L. Zhang, *J. Am. Chem. Soc.* **2015**, *137*, 6393.